Arabian Journal of Chemistry (2023) **16**, 104904

King Saud University

Arabian Journal of Chemistry

www.ksu.edu.sa
www.sciencedirect.com

ORIGINAL ARTICLE

Cs_2SnI_6 perovskites nanostructures as excellent photocatalytic degradation of organic dye pollutants in water under visible light: Synthesis and characterization

Fatemeh Yousefzadeh [a], **Mojgan Ghanbari** [a], **Elmuez A. Dawi** [b], **Masoud Salavati-Niasari** [a,*]

[a] *Institute of Nano Science and Nano Technology, University of Kashan, Kashan, P. O. Box.87317-51167, Islamic Republic of Iran*
[b] *Nonlinear Dynamic Research Center (NDRC), College of Humanities and Sciences, Ajman University, P.O. Box 346, Ajman, United Arab Emirates*

Received 17 September 2022; accepted 8 April 2023
Available online 20 April 2023

KEYWORDS

Perovskites;
Semiconductor;
Co-Precipitation method;
Cs_2SnI_6 nanostructures;
Visible-Light-Driven photocatalysis

Abstract Pollution of surface waters containing chemical dye combinations and/or biological materials can have adverse effects on human health and other organisms, even in small quantities. The photocatalytic oxidation procedure has been widely regarded as a commercially viable method of removing environmental pollutants. In recent research, Caesium-hexaiodostannate nanostructures (Cs_2SnI_6) were prepared through a co-precipitation approach and their photocatalytic performance was analyzed. A number of surfactants were examined for their influence on the structure, purity, and morphology of the sample. It was found in the SEM data that the presence of surfactants has a negative impact on the morphology, which may be due to the inability to remove surfactants by calcination at high temperatures. Photocatalytic activity of Cs_2SnI_6 catalysts was demonstrated over a variety of organic dyes, including methylene blue (MB), rhodamine b (RhB), methyl orange (MO), and methyl violet (MV). Upon exposure to visible light for 180 min, 5 ppm methylene blue showed the greatest degradation (84.0%). Cs_2SnI_6 nanostructures are being applied for the first time in photocatalytic applications. Due to their wide bandgap (1.7 eV) in the visible region, they may be a suitable candidate for water purification. Moreover, the results indicated that the efficiency of photocatalysis was affected by various parameters, including pH, dye concentration, dye types, catalyst dosages, and surfactants. In the recyclability test,

* Corresponding author.
E-mail address: salavati@kashanu.ac.ir (M. Salavati-Niasari).
Peer review under responsibility of King Saud University.

Production and hosting by Elsevier

https://doi.org/10.1016/j.arabjc.2023.104904

Cs_2SnI_6 nanostructures were found to be stable, and the removal efficiency was reduced by 6.9% after the fifth run.

1. Introduction

It is widely accepted that population growth and industrial development are not only reducing clean water resources, but also causing degradation in water quality, which negatively impacts the health and safety of humans and other living organisms (Ajibade & Oluwalana, 2021; Zhang et al., 2022). Furthermore, wastewater contains a variety of organic compounds, including dyes, medicines, and personal care products that are often resistant to natural degradation (Li et al., 2022a). Although their concentration is very low, the damage they cause cannot be ignored (Li et al., 2022b). Diverse industries can release sewage directly into the environment, which can have a negative impact on aquatic life and human health (Sharwani et al., 2021). In order to purify them, a great deal of energy must be expended (Khan, 2021). As a result of chemical spills, agricultural runoff, and industrial effluent, toxic coloring agents are discharged into water systems (Islam et al., 2021; Lavanya et al., 2014). In many countries, regulatory authorities and societies face problems as a result of stability, acute toxicity, and durability in the ecosystem for long periods of time (Kubra et al., 2021). During the dyeing process, a significant amount of water is used and discharged into the ecosystem on a regular basis. Textile dyeing industry effluents, which contain carcinogenic and hazardous dyes, are poisonous to mammals, aquatic microorganisms, and fish, threaten to destroy the aquatic environment by destroying hydrophyte plants in their photosynthesis (Fu et al., 2011; Nasar, 2021). Increasing amounts of chemical oxygen from dye wastewater produced by photographic and textile industries are causing an ecological crisis due to their unsuitable color, toxicity, and resistance to biological, photochemical, and chemical degradation (Kumar et al., 2021; Waheed et al., 2021; Zhou et al., 2021). Most colorants are mutagenic, carcinogenic, and life-threatening. Dye can cause allergic reactions, such as respiratory infections, contact dermatitis, respiratory tract irritation, and even cancers of the liver, bladder, and kidney. Highly poisonous textile dyes can reduce the penetration of light in water, reduce the transparency and quality of water, and affect the photosynthetic behavior of hydrophytic plants, leading to a lack of oxygen in aquatic environments (Al Kausor & Chakrabortty, 2021). Contaminants such as these pose a great threat to the aquatic ecosystem as well as to human health. In an attempt to remove these pollutants, methods such as ozonation, biochemical treatment, and electrochemical oxidation have been used, but they are hindered by several limitations (Sui et al., 2020; Xu et al., 2022). The purification of these toxic colorants in organic micro-pollutants (OMP) has always attracted the attention of scientists. As a general rule, conventional methods of eliminating organic dyes do not meet the standards for water quality and are not compatible with existing water sources. Due to its ability to remove toxic pollutants entirely to mineral acids, water, and carbon dioxide, photocatalysts based on semiconductors have gained considerable attention for their use in the refinement of environmental contaminants in sewage (Arunachalam et al., 2021; Ghanbari & Salavati-Niasari, 2018; Liu et al., 2011; Zhang et al., 2007).

A semiconductor-based photocatalysis technology is the most lucrative due to its potential applications in a variety of fields, particularly in the decomposition of toxic contaminants(Pasternak & Paz, 2013; Wu et al., 2010). As a result of the advancement of nanotechnology, photocatalysis has become one of the most important approaches in wastewater treatment. Two aspects of issues related to water are of particular interest to researchers: first, simple and low-cost access to clean drinking water, and second, appropriate and low-cost treatment of effluents to limit environmental harm. All around the world, significant amounts of research are conducted daily in these fields. Several technologies and methods are being developed and optimized for the treatment of water and wastewater, including the use of photocatalysts. The process of photocatalysis involves the use of a semiconductor material that is capable of producing electron holes in the presence of visible or ultraviolet light (Karami et al., 2021).

Perovskites are characterized by a wide range of structural and compositional variations that offer many possibilities for overcoming the challenges posed by $MPbX_3$ and $MSnX_3$ perovskites halides. As with perovskites oxides, halide perovskites are also available (Attfield et al., 2015). The BI6 octahedron undergoes a phase transition that reduces symmetry during cooling, resulting in a coordinated tilt that affects its conductivity and bandgap (Amat et al., 2014; Chung et al., 2012; Moller, 1958; Swainson et al., 2015). Besides, halides can create ordered double perovskites with the general equation $M_2N'N''X_6$, wherein the rock-salt ordering of the N' and N" metals are present. The order is usually due to an extensive charge difference between the two metals (Anderson et al., 1993). Substitution of one site of N cation with an empty site in the $M_2N'N''X_6$ double perovskite results in the vacancy-ordered double perovskites, M_2NX_6. Commonly mentioned as antifluorite compounds, these defective perovskites embrace the K_2PtCl_6 structure type, which is defined as isolated $[BX_6]^{2-}$octahedra units bridged with M^+ cations (Maughan et al., 2016; Wang et al., 2019). There are some similarities between M_2NX_6 perovskites and MNX_3 perovskites. A close-packed ionic lattice similar to that of ABX_3 perovskites is maintained, despite the removal of all other $[BX_6]$ octahedrons. Additionally, vacancy-ordered structures undergo coordinated octahedral tilts and rotations during phase transitions, reducing their symmetry during the cooling process (Abrahams et al., 1989; Henkel et al., 1980; Lee et al., 2014; Saparov et al., 2016). Cs_2SnI_6 exhibits a cubic structure at ambient temperature with a space group of Fm_3m, as indicated by its radius ratio $\sim$ of 0.94 (Shin et al., 2019). The mixture is characterized by n-type electrical conductivity, strong visible light absorption, moisture stability, and air stability, which are all beneficial for photovoltaic devices (Lee et al., 2014; Saparov et al., 2016). One of the most critical factors in the selection of light for photocatalysis is the catalyst bandgap. We have conducted a wide range of photocatalysis research using semiconductor nanoparticles in our lab. In this field, new materials are constantly being created, optimized, and utilized. It is known that Cs2SnI6 has a bandgap that is suitable in the visible region; 1.622 eV (Qiu et al., 2016). Because of its low cost, environmental friendliness, and high efficiency, the cesium tin iodide perovskite semiconductor (Cs_2SnI_6) has recently attracted considerable attention as a semiconductor for light-emitting diodes, solar cells, catalytic electrodes in fuel cells, superconductivity, sensors, and photodetectors. (Rasukkannu et al., 2018).

As one of the primary objectives of this paper, Cs_2SnI_6 nanocomposite will be synthesized in a simple and cost-effective manner. Synthesis of nanocomposite Cs_2SnI_6 was accomplished by co-precipitating. The characterization of Cs_2SnI_6 has been performed using a variety of methods, including XRD, SEM, EDS, TEM, BET, and DRS. As part of this study, Cs_2SnI_6 was examined for its photocatalytic activity. It is a first-of-its-kind study that will investigate pH, dye type, catalyst dosage, dye concentration, scavenger type, and surfactant type.

2. Experimental

2.1. Materials and characterization

The reagents used in this study were all of analytical quality. Potassium iodide (KI), Cesium chloride (CsCl), Tin(IV) chloride pentahydrate ($SnCl_4{\cdot}5H_2O$), Polyethylene glycol (PEG-6000), Sodium dodecyl sulfate (SDS), polyvinyl pyrrolidone (PVP-25000), sodium dodecylbenzene sulfonate (SDBS), Ethylenediamine tetra acetic acid (EDTA), Sodium salicylate (NaHSal), Benzoic acid (BA), 1,4-Benzoquinone (BQ), sodium azide (NaN_3), were purchased from Merck Company and applied without additional purification. We employed methyl violet ($C_{24}H_{28}N_3Cl$), rhodamine B ($C_{28}H_{31}C_lN_2O_3$), methyl orange ($C_{14}H_{14}N_3NaO_3S$), and methylene blue ($C_{16}H_{18}C_lN_3S$) as contaminants for studying the photocatalytic behavior of Cs_2SnI_6 nanostructures.

XRD (X-ray diffraction) patterns were collected using a Philips diffractometer with X'PertPro monochromatized Cu K radiation (λ = 1.54) to determine the type of structure and purity of the as-synthesized nanoparticles. The shape and distribution of nanoparticles were examined using FESEM (field emission scanning electron microscopy) (Mira3 TESCAN). The nanoparticles were evaluated by transmission electron microscopy using a JEM-2100 TEM, and by energy dispersive spectrometry using a Philips XL30 microscope. Catalyst specific surface areas were calculated using the Brunauer-Emmett-Teller (BET) technique. To determine adsorption/desorption, an automated gas adsorption analyzer (Tristar 3000, Micromeritics) was used to pump liquid N_2 at −196 °C.

2.2. Synthesis route

Precursors must be prepared before Cs_2SnI_6 nanoparticles can be synthesized. SnI4 was synthesized using the co-precipitation method in the first step. A solution of 1.5 mmol $SnC_{l4}{\cdot}5H_2O$ and a solution of 3.0 mmol KI were dissolved in distilled water in two beakers and then combined. Second, stoichiometric amounts of CsCl (1.5 mmol) and LiI (1.5 mmol) were dissolved in distilled water in two beakers for the synthesis of CsI (if surfactant (1.5 mmol) was used, it was added at this point). Following the mixing and stirring of the solutions, the reaction was carried out for 15 min. CsI solution was added to a beaker containing SnI_4 and the solution turned yellow. Following 30 min of stirring, the precipitate was washed several times with ethanol to remove residual surfactant and dried in an oven at 65 °C. It is apparent from the black precipitate obtained that nanoparticles have been formed (Scheme 1). A variety of tests and analyses were conducted on the precipitate resulting from the reaction.

2.3. Photocatalyst process

In order to conduct the photocatalysis procedure, different amounts of the optimum samples were added to 100 ml of dye solution at different concentrations (such as 5, 10, and 15 ppm). During the photocatalysis process, the solution was aerated for 20 min. The photocatalytic process was carried out using an Osram light (400 W) with a wavelength ranging between 400 and 780 nm. As soon as the aeration process had been completed, the first sample was collected. To reach equilibrium, the mixture containing catalyst and dye was blended in the dark for 30 min before turning on the lamp below visible rays. The reaction medium was then illuminated with visible light. Despite the fact that the initial sampling was conducted after 30 min, subsequent samplings were conducted every 30 min. Photocatalysis was performed at room temperature without external light or catalyst, and after 120 min, hardly any dye was degraded without light and catalyst. A UV–visible spectrophotometer was used to measure the absorbance of the collected samples in order to verify the discoloration. The percentage of discoloration was calculated by using the following formula (Eq. 1), where A_0 represents the quantity of dye absorption before and after exposure to light, and A_t represents the amount of dye absorption after exposure to light:

$$\%\text{Decolorization} = \frac{A_0 - A_t}{A_0} \times 100 \quad (1)$$

2.4. Cyclic voltammetry (CV) test

Electrochemical energy storage capacity and attributes of products were assessed using the cyclic voltammetry (CV) technique. The probe solution of potassium ferricyanide/potassium ferrocyanide ($K_3(Fe(CN)_6)/K_4(Fe(CN)_6)$) in the 0.1 M phosphate buffer solution (pH = 7.2) was applied for CV test at the scan rate of 0.1 Vs^{-1}. Electrochemical cells were thermostatized at 25 °C in 2 M KOH electrolyte. These electrodes consist of the working electrode, Pt electrode, and Ag/AgCl electrode. In order to prepare the working electrode without a binder, a thin layer of as-fabricated materials was coated on a copper substrate using the drop cast method. Through the current between the as fabricated electrode and the counter electrode, the potential of the fabricated working electrode was measured against the reference electrode.

3. Results and discussion

3.1. Characterization of Cs_2SnI_6

The XRD pattern of Cs_2SnI_6 as synthesized is shown in Fig. 1a. Each diffraction peak is associated with cesium tin iodide with JCPDS No. 073–0330 having a cubic crystal structure (space group = $Fm^{-3}m$). The effect of several surfactants on the purity and structure of Cs_2SnI_6 was studied, including SDS, SDBS, NaHSal, PEG6000, PVP, and EDTA. Fig. 1b and 1c illustrate the XRD pattern of Cs_2SnI_6 prepared with SDS and SDBS as anionic surface active agents. Tin iodide with JCPDS No. 075–1559 was composed as a by-product along with the main phase. A small amount of unknown phase was also formed in the presence of SDBS. When sodium salicylate (NaHSal) is used as a surface-active agent, it can result in certain impurities such as unknown phase and SnI4 in the sample (Fig. 1d). In Fig. 1e and 1f, polymeric surface-active agents, such as PEG6000 and PVP, were applied in order to obtain pure Cs_2SnI_6 with high crystallinity. Furthermore, Cs_2SnI_6 and SnI_4 were formed as a result of EDTA acting as a chelating agent. The pure phase of Cs_2SnI_6 was obtained under three different conditions, including the absence of surfactants and the presence of polymeric agents such as PVP and

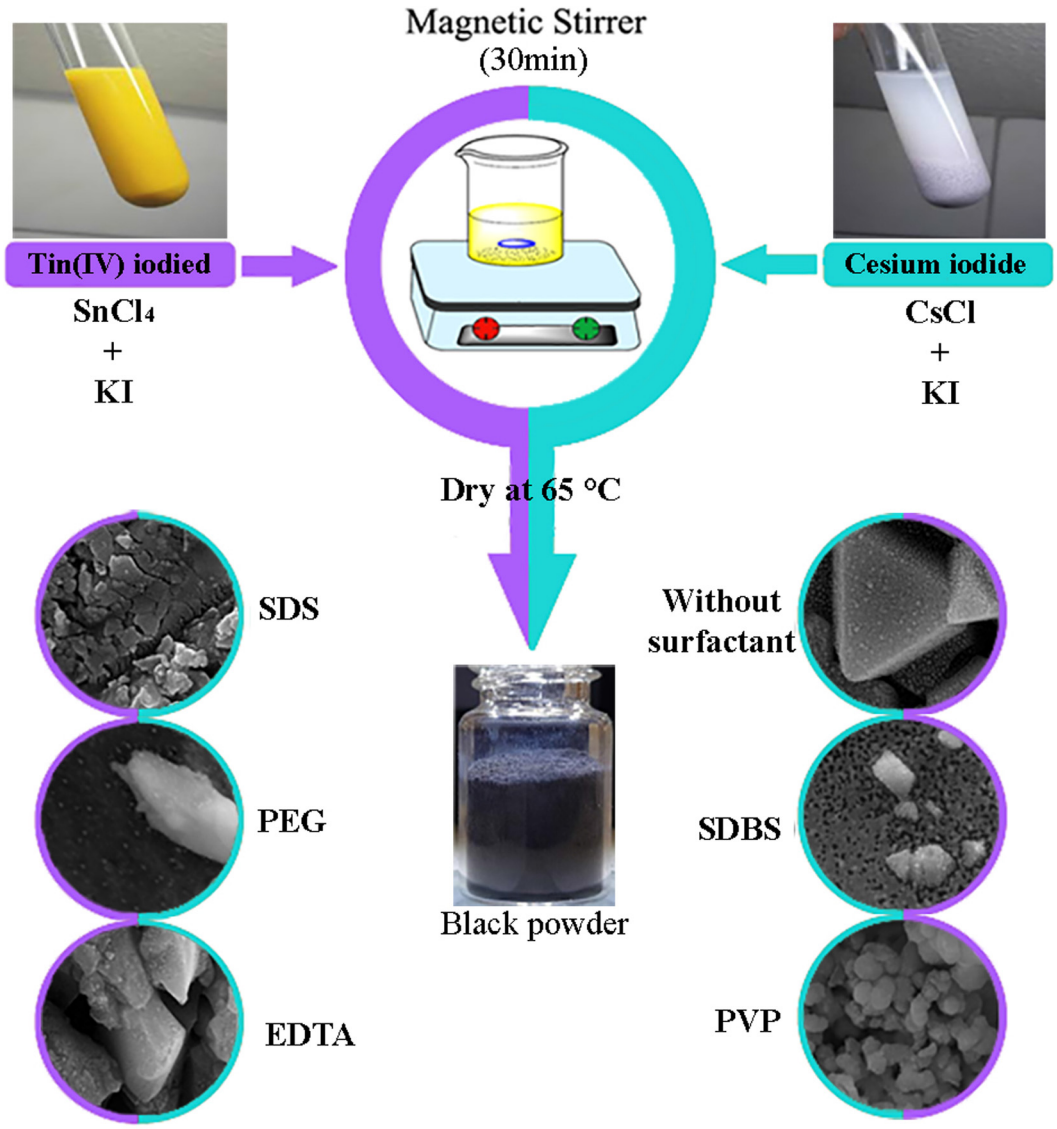

Scheme 1 Schematic diagram of the fabrication of Cs_2SnI_6 nanostructures.

PEG6000. Based on the Scherrer equation, the crystal size of the samples was determined to be between 36 and 54 nm (Table 1). (Karami et al., 2021; Tahir et al., 2020).

$$D = \frac{0.9\lambda}{\beta \cos\theta} \tag{2}$$

The morphology of the synthesized nanoparticles was examined using SEM. A variety of surfactants were used to prepare nanoparticles, as previously mentioned. It was expected that the morphologies of nanoparticles would differ due to the use of different types of surfactants. The images in Fig. 2a and b illustrate synthesized nanoparticles without surfactants. Particles are arranged in a regular pattern and are in different polyhedral states. As can be seen in the 200 nm scale image, the polyhedral structures are formed by tiny nanoparticles. In this sample, a bulk nanostructure is observed. In contrast, different surfactants formed agglomerates of considerable size, contrary to expectations. In the case of SDS, an anionic surfactant (Fig. 2c and d), flakes were formed without being properly distributed. In the presence of SDBS, an anionic surfactant, small nanoparticles with some agglomerations were obtained (Fig. 2e and f). PEG-6000, an anionic (polymeric) surfactant, was used to produce bulk nanostructures in Fig. 2g and h. Further, when PVP was used as a polymeric surfactant, the d-spheres appeared quite clear (Fig. 2i and j). As in sample 1, tiny particles are observed on the surface of the nanoparticles that form the sphere in this sample (sample 6). EDTA was also used as a chelating agent in the preparation of the bulk nanostructures (Fig. 2k and l). As a result of the use of various surfactants, diverse morphologies are produced with larger sizes and irregular shapes. The synthesis of nanostructures with controlled size, shape, and aspect ratio has made extensive use of surfactants of different ionic phases (cationic, anionic, and non-ionic) (Carswell et al., 2003). In general, surfactants are thought of as capping agents, structure guiding agents, or templates. Every surfactant has its own mechanism for preparing nanostructures. During the fabrication procedure, surfactants are adsorbed to the growing

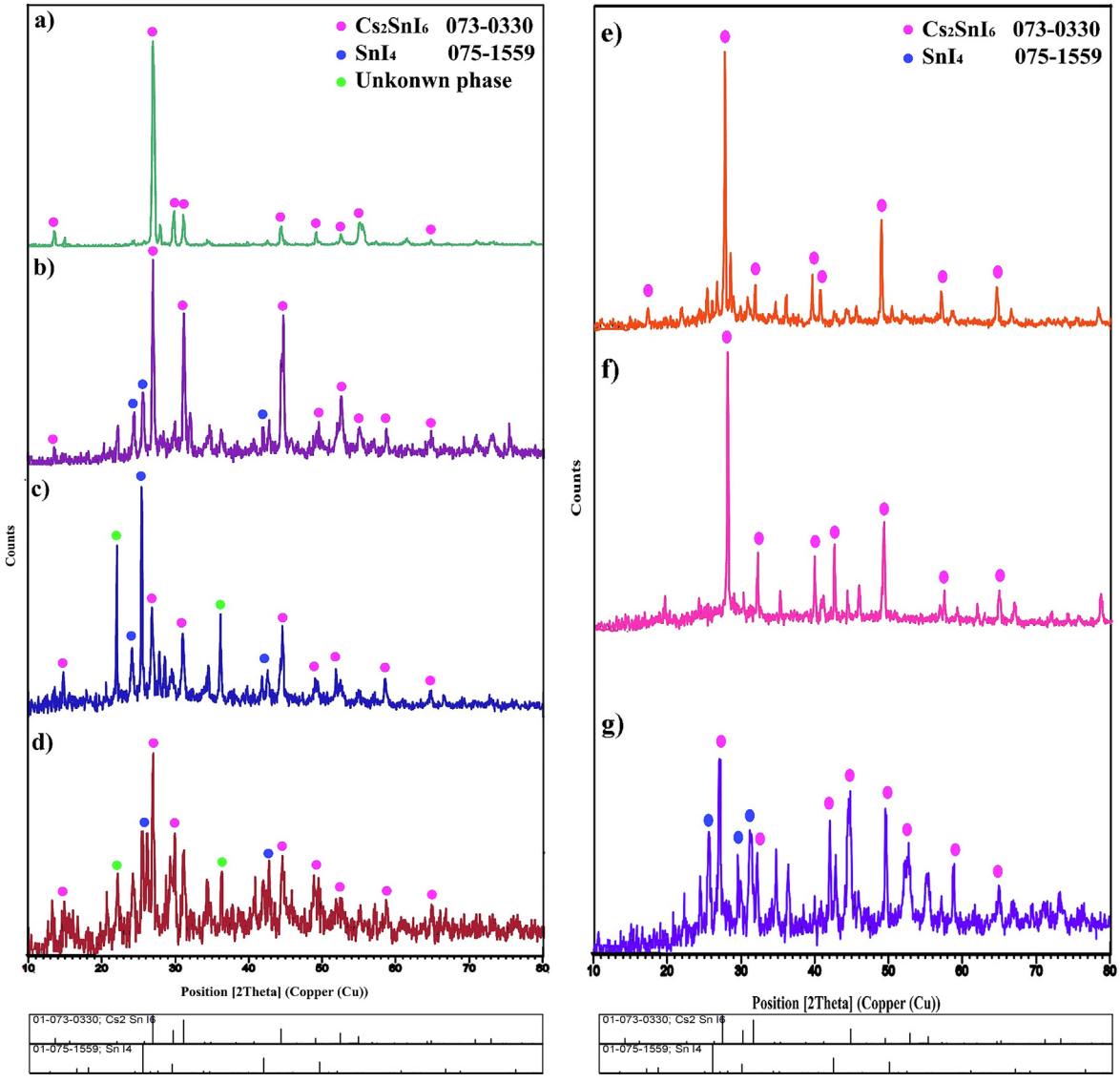

Fig. 1 XRD patterns of Cs_2SnI_6 nanostructures (samples 1–7).

Table 1 Fabrication conditions for Cs_2SnI_6 nanostructures.

Sample No.	Type of Capping Agent	Products	Crystal Size (nm)
1	–	Cs_2SnI_6	40.1
2	SDS	Cs_2SnI_6, SnI_4	40.7
3	SDBS	Cs_2SnI_6, SnI_4, Unknown	43.2
4	NaHSal	Cs_2SnI_6, SnI_4, Unknown	51.3
5	PEG6000	Cs_2SnI_6	36.6
6	PVP	Cs_2SnI_6	48.7
7	EDTA	Cs_2SnI_6, SnI_4	54.6

crystal and, depending on the starting material concentration and surfactant characteristics, they can limit the growth rate of crystal faces, thereby assisting in the regulation of crystal sizes and shapes (Santra et al., 2001). It is possible that some surfactants may adversely affect the structure and morphology of products. It is possible that the lack of particles with the appropriate morphology and size is due to the inability to remove surfactants through calcination at high temperatures. The HRTEM images of Cs_2SnI_6 are shown in Fig. 3. In accordance with SEM results, the particles are arranged in a regular pattern. These photographs clearly demonstrate the coexistence of tiny nanoparticles. In order to demonstrate the high crystallinity of Cs_2SnI_6, parallel lines were specified for the crystal planes. The lattice planes are presented by the interplanar space of 3.2 Å, which conforms to the crystal planes (2 2 2) of Cubic Cs_2SnI_6 crystals.

Similarly, Fig. 4(a-e) illustrates the EDS mapping images and EDS spectrum of Cs_2SnI_6. As shown in Fig. 4(a-d), the related maps of I, Sn, and Cs elements exhibit glossy zones similar to the calcification zones. It is evident from the EDS spectrum of Cs_2SnI_6 that the product contains I, Sn, and Cs elements, indicating its high purity. In this spectrum (Fig. 4e), the W% and A% of each element are clearly visible.

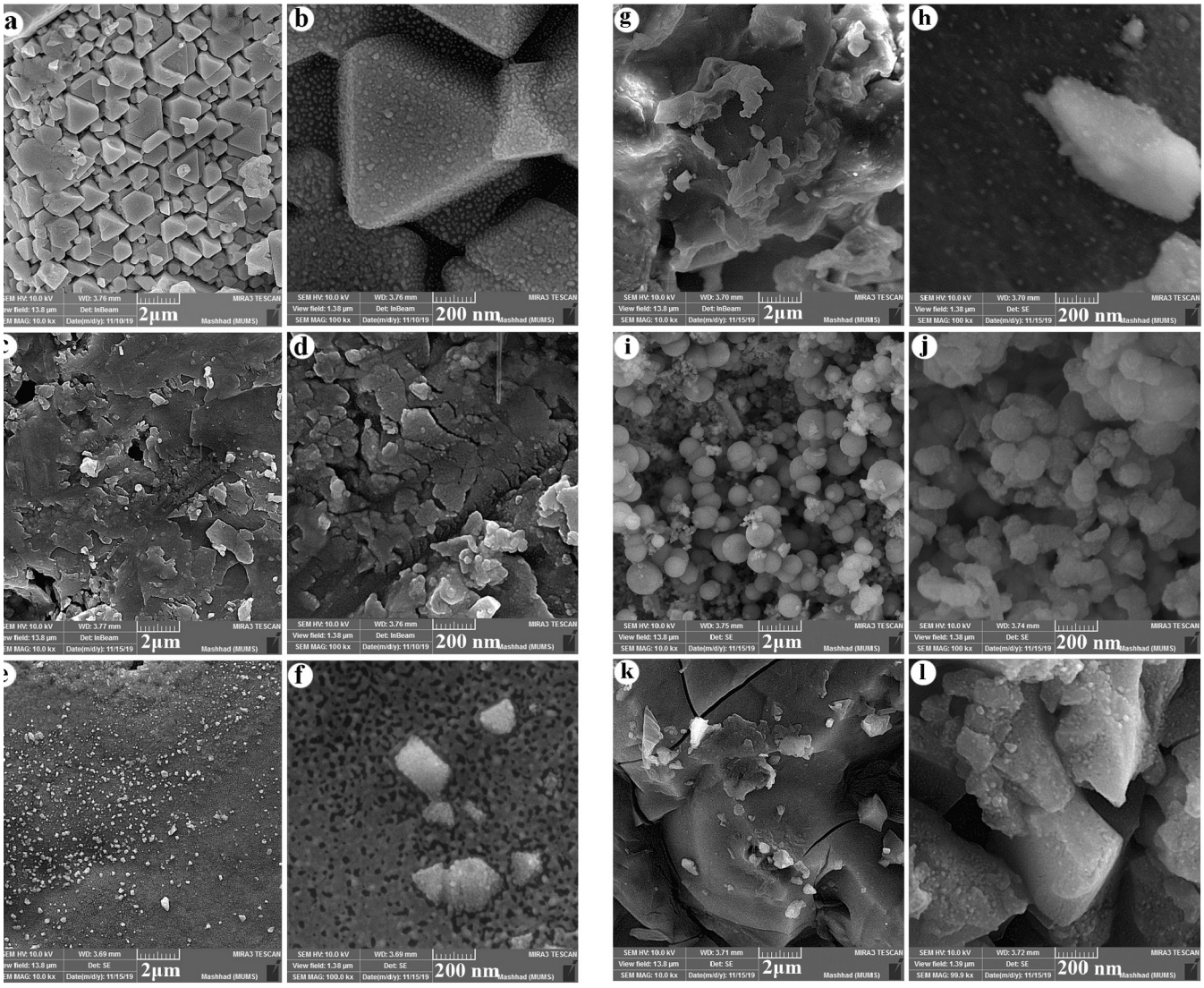

Fig. 2 FESEM micrographs of Cs_2SnI_6 nanostructures (samples 1–7).

It is also important to note that the Cs_2SnI_6 sample lacked any other elements. The Fig. 4f illustrates the N_2 adsorption–desorption isotherm of Cs_2SnI_6, along with its associated pore size distribution profile. A microporous or mesoporous material is implied by the isotherm of type III (Karami et al., 2021). The isotherm exhibits a H3-type hysteresis loop, which corresponds to groove pores formed by flack particles in a nonrigid generation (Chen et al., 2018). Total pore volume at p/p0 = 0.989 was obtained at 0.018 cm^3g^-1, average porosity diameter was estimated at 17.6 nm, and specific aBET was achieved at 4.1 m^2g^{-1}. Fig. 4g displays the porous size distribution obtained from the desorption part of the isotherm via the BJH technique. It can be seen that the pore distribution of the generated Cs_2SnI_6 is multi-peak.

DRS spectrum of Cs_2SnI_6 (sample 1) is shown in Fig. 4h. The absorption peaks from 200 to 400 nm verify the semiconducting properties of the prepared Cs_2SnI_6. The calculated bandgap was determined using the following equation (Ghanbari & Salavati-Niasari, 2018):

$$(\alpha h\upsilon)^{1/r} = \beta(h\upsilon - Eg) \tag{3}$$

that α is absorption constant; hυ is the energy of the photon (eV); r is 2 for the direct or 1/2 for the indirect transitions; Eg is bandgap, and β is constant. Fig. 4i indicates the plot of $(\alpha h\upsilon)^2$ vs. hυ for Cs_2SnI_6 (sample 1). Bandgap was calculated by partially linear extrapolating this curve to a point $(\alpha h\upsilon)^2 = 0$ to be 1.7 eV.

The CV diagram of Cs_2SnI_6 is shown in Fig. 4j. The CV characteristics curves was used to calculate the conduction band (CB) and the valence band (VB).

$$CB(or\ VB)(eV) = -4.8 - \left(E - E_{1/2}\right)(eV) \tag{4}$$

where E is the redox potential peak (Mora-Sero et al., 2013) and $E_{1/2}$ is the formal potential ($E_{1/2}$ = 0.09 V) against the Ag/Ag^+ system (Qin et al., 2015). Energy values for CB and VB are − 4.22 and − 5.71 eV, respectively. The Cs_2SnI_6 VB and CB energy levels are consistent with previously published values (Zhou et al., 2021).

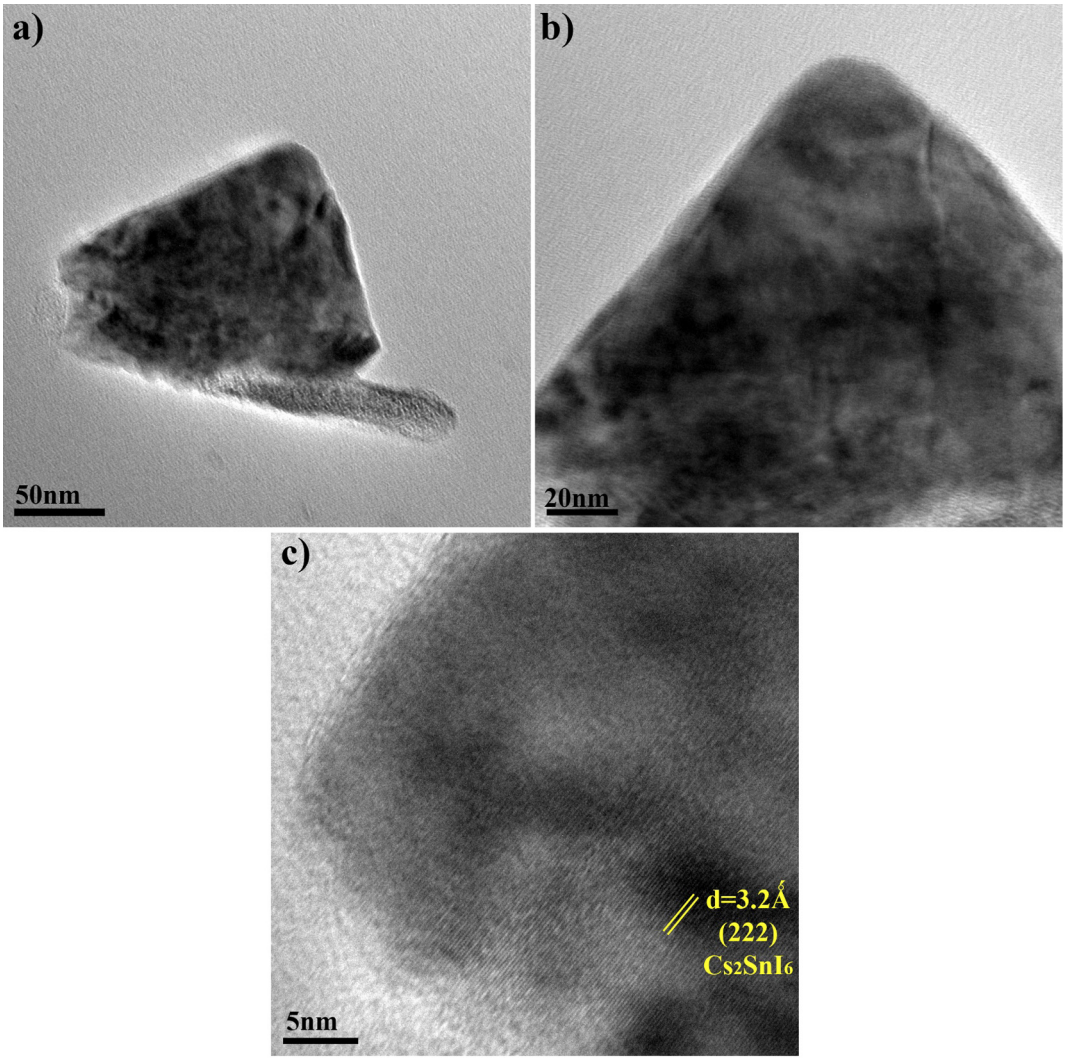

Fig. 3 TEM micrographs of Cs_2SnI_6 nanostructures (sample 1).

3.2. Photocatalytic behavior

To fully understand the photocatalytic process, several factors must be considered, including light source, dye types, pH, catalyst dosages, dye concentrations, etc. (Ghanbari & Salavati-Niasari, 2018). In order to assess the effect of visible irradiation on the degradation of MB at ambient temperature, i.e., photolysis, a control test was conducted first. The dye was rather degraded in visible light after 180 min of irradiation, as illustrated in Fig. 5a (about 6 percent). The experiment was then conducted in the dark in order to evaluate the adsorption of dye on the catalysts. A UV–Visible spectrometer was used following centrifugation to monitor the aliquot at 10 min intervals for 60 min. Adsorption capacity (Qt) is expressed as earlier by Ajibade et. al. (Ajibade & Oluwalana, 2021):

$$Q_t = \left(\frac{C_0 - C_t}{W}\right) V \tag{4}$$

where C_0, C_t (mg/L), W, and V are the initial dye concentration, concentration at a specific time, weight of the adsorbent, and volume of dye, respectively. The Cs2SnI6 nano photocatalyst reached equilibrium adsorption capacity in the photocatalytic process after 30 min for all dosages (Fig. 5a). After 30 min, the adsorption capacity remained stable, indicating that equilibrium between adsorption and desorption had been achieved. We used this procedure to determine the amount of dye adsorption on Cs_2SnI_6 nanoparticles. According to the findings, approximately 15% of the degradation had been observed after 180 min (Fig. 5b). Rather, this number represents dye adsorption on the catalyst surface, which was further examined using BET analysis. The degradation of methylene blue is not possible without a catalyst and visible light. In this study, both light and catalyst play a crucial role in the elimination of organic contaminants.

3.2.1. Organic pollutant types

An illustration of the influence of dye species on Cs_2SnI_6 nanoparticles can be found in Fig. 5c. The removal efficiency of MB, RhB, MV, and MO is approximately 72.9, 61.9, 27.1, and 23.7%, respectively. Based on the results of this study, it can be concluded that the efficiency of cationic organic pollutants is greater than that of anionic dyes, since

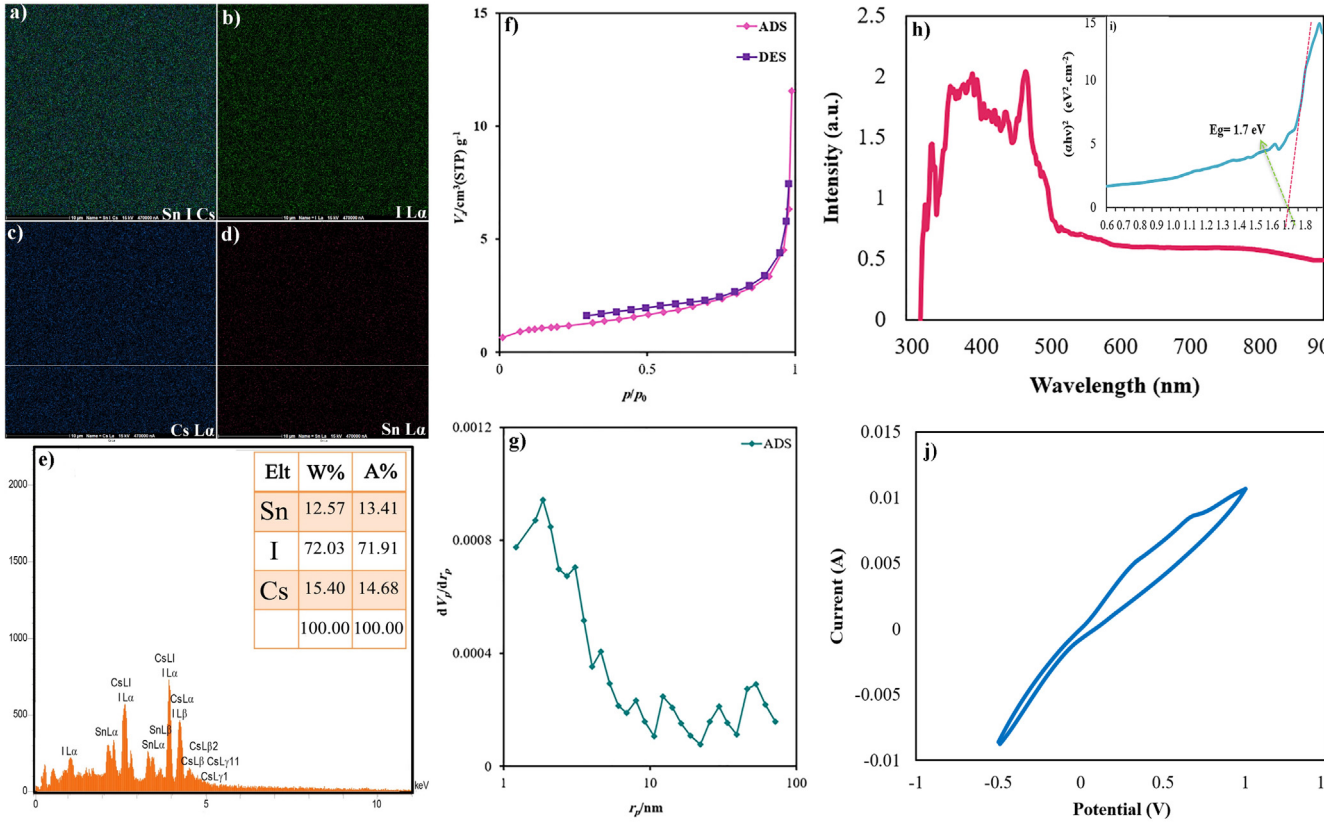

Fig. 4 (a-d) EDS mapping, e) EDS spectrum, f) N_2 adsorption/desorption isotherm, g) BJH plot, h) DRS spectrum, i) $(\alpha h\upsilon)^2$ vs. hυ plot, and j) cyclic voltammetry of Cs_2SnI_6 nanostructures (sample 1).

iodide ions (I^-) are negatively charged within the nanostructure. Fig.10a illustrates how pH solution affects MB discoloration.

3.2.2. *Effect of pH of the solution*

We examined the impact of the pH of the solution on the removal efficiency (Fig. 5e). In acidic (pH = 3), neutral (pH = 6), and alkaline (pH = 10) media, the degradation efficiency was approximately 34.8%, 52.6%, and 84.0%, respectively. Based on these results, alkaline media (pH = 10) showed the greatest increase in efficiency. Because methylene blue is a cationic dye, it acts efficiently at pH > 7 by increasing the concentration of OH groups in the solution. It is reasonable to assume that the concentration of OH groups will increase with increasing pH. In other words, the generation of OH in the solvent will be extended, and the photocatalytic efficiency will be enhanced.

3.2.3. *Cs_2SnI_6 doses*

Moreover, the removal efficiency yield of Cs_2SnI_6 (sample 1) was examined in relation to its dose. As noticed in Fig. As shown in Fig. 6a, the catalytic efficiency is largely dependent on the catalyst dosage. Changing the nanocatalyst dosage from 50 to 70 mg enhanced the degradation efficiency of Cs_2SnI_6 from 72.9 to 78.5%. By increasing the nanocatalyst dosage from 70 to 100 mg, the catalytic yield was increased from 78.5 to 84.0%. Therefore, increasing the Cu_2HgI_4 doses increases the surface area of the catalyst and enhances dye adsorption on Cs_2SnI_6.

3.2.4. *Concentration of organic pollutants*

Fig. 6c illustrates the effect of different dye concentrations (5, 10, and 15 ppm) of MB after 180 min. A decrease in dye concentration from 10 ppm to 5 ppm increases the degradation percentage from 71.0% to 84.0%, while an increase in dye concentration reduces dye decolorization. By increasing pollutant concentrations from 5 ppm to 15 ppm, the removal efficiency declined from 84.0 to 63.0%. The binding sites on the Cs_2SnI_6 surface are occupied by a large number of MB molecules at 15 ppm. It is evident that enhancing the dye concentration reduces the degradation percentage (de Luna et al., 2013).

3.2.5. *Kinetic study*

Langmuir–Hinshelwood mechanism was used to calculate the rate constants (eq.4) of the photocatalytic reaction of organic dyes (Kumari & Meena, 2020). Where k is the rate constant (min^{-1}) for Pseudo-first order reaction; C_0 is the primary concentration of contaminating solution; and C is the pollutant concentration at t time. The rate constant (k) for Pseudo-first order reaction has been defined from $\ln(C_0/C)$ linear correlations versus time. Fig. 6b, 6d, and 6f indicate that the maximum photocatalytic degradation is obtained at a greater rate constant (k = 0.0098 min^{-1}).

$$kt = ln(C_0/C) \tag{5}$$

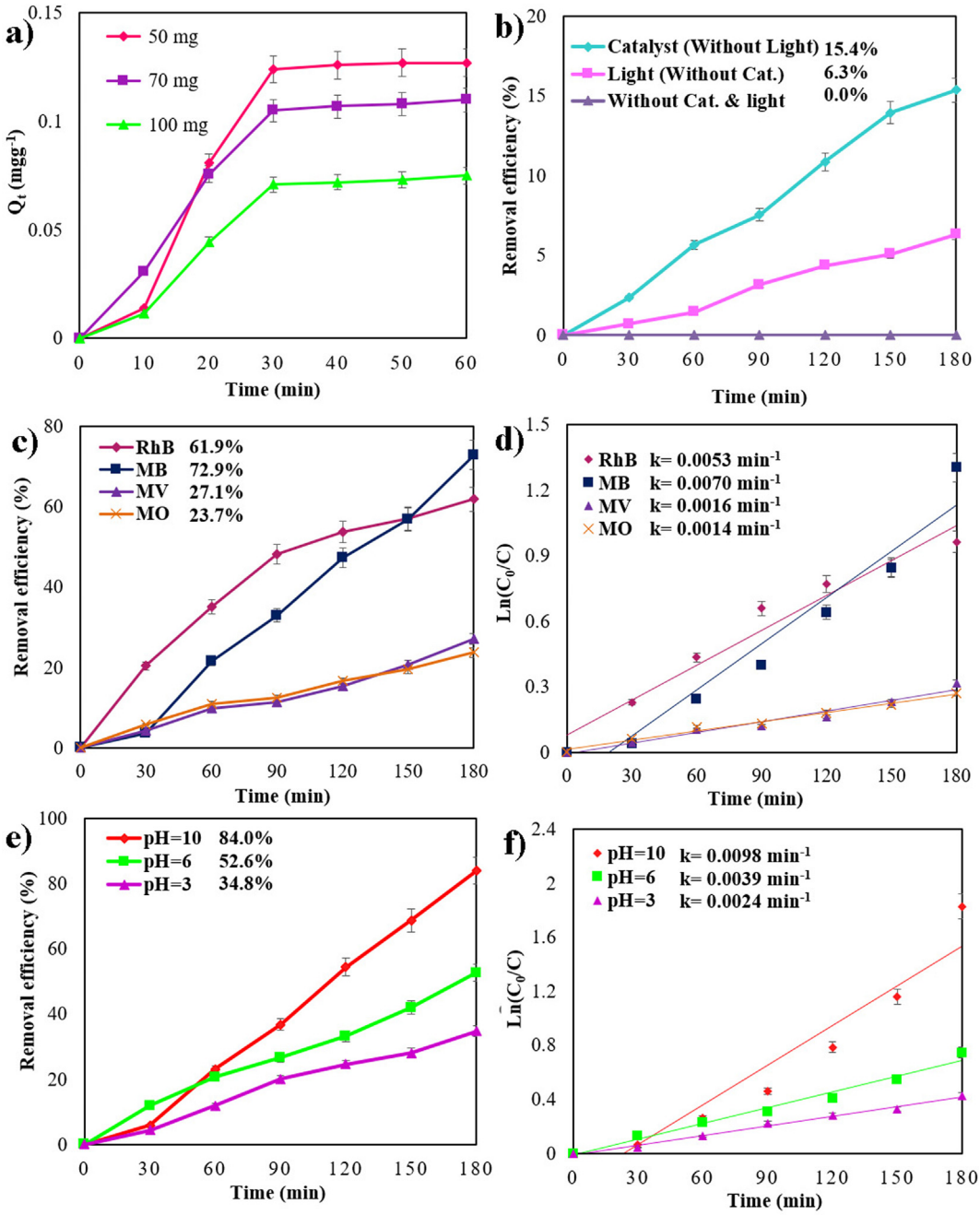

Fig. 5 A) time profile adsorption capacity in different catalyst dosages, b) effect of light and catalyst on the photocatalytic degradation, photocatalytic degradation of different dyes over sample 1 and Plots of ln(C_0/C) vs time (c and d), photocatalytic degradation in three different pH over sample 1 and Plots of ln(C_0/C) vs time (e and f) under visible-light.

3.2.6. Effect of surfactant

Fig. 6e illustrates MB photodegradation in the presence of various surfactants. Due to the better interaction between MB, a cationic dye, and anionic surfactants, the removal efficiency is improved in the presence of anionic surfactants such as SDS (64.4%) and SDBS (91.2%). There are three factors that contribute to the excellent photocatalytic activity of Cs2SnI6 in the presence of SDBS: i) The presence of SnI4 with a band gap of 1.52 eV results in a narrower band gap. According to the XRD pattern of sample 3 (SDBS), SnI4 peak intensity is higher in sample 3 than in sample 2 (SDS), indicating that sample 3 contains a greater amount of SnI4. Due to the narrower bandgap, more radiation can be used to excite more charge carriers, leading to enhanced photocatalytic activity. The particles that are formed in the presence of SDBS are smaller than those formed by SDS, resulting in a larger specific surface area, as shown by the FESEM images of samples 2 and 3. It is generally accepted that a photocatalyst's specific surface area is closely associated with its photocatalytic activity. A higher surface area not only boosts the contact area between photocatalyst and the reactant, but it also supplies more active sites through the photocatalytic operation, which improves photo-

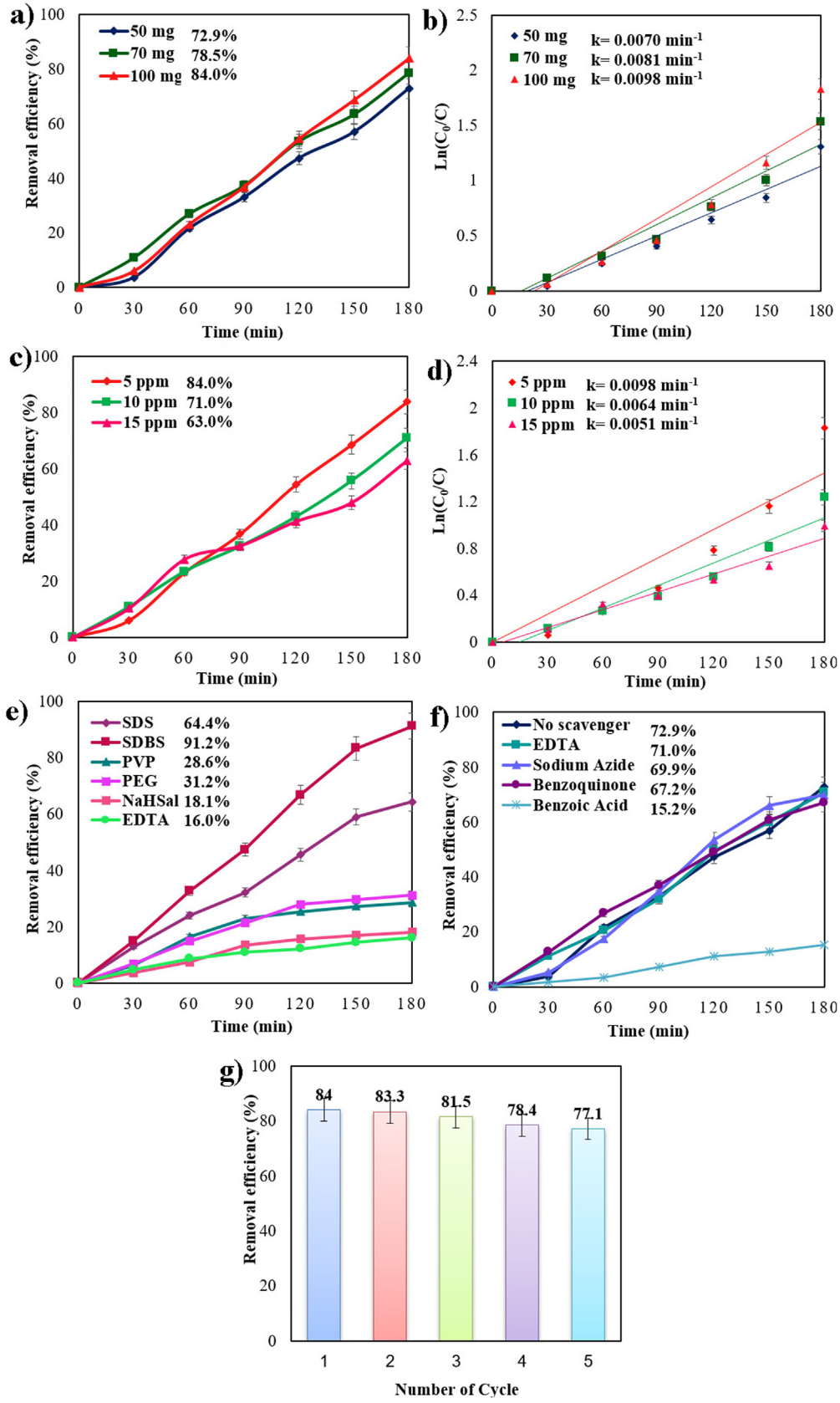

Fig. 6 Photodegradation of various organic dyes over sample 1 and Plots of $\ln(C_0/C)$ vs time in three different catalyst dosages (a and b), concentration of organic pollutants (c and d), different surfactants (e), effect of various scavengers (f), and cycling runs in the photocatalytic degradation of 5 ppm MB (g) under visible light.

catalytic performance (Song et al., 2015). iii) smaller particle size. The photoinduced charge carriers have a shorter diffusion distance due to the smaller particle size, which causes them to migrate quickly to the catalyst surface and successfully separate (Peng et al., 2015).

3.2.7. Mechanism study through scavenger test

In aqueous catalyst suspensions, it has been completely demonstrated that valence band holes (h^+) and conduction band electrons (e-) are produced when light energy exceeds the band gap of the catalyst (1.7 eV). Using photoinduced electrons, the colorant can be reduced or reacted with electron acceptors, such as O_2 dissolved in water or adsorbed on the catalyst surface, thereby reducing it to $O_2^{\cdot-}$ (radical of superoxide anion). Photoinduced holes can react with H_2O and OH^- to form $OH^{\cdot}$ radicals or oxidize organic dyes to produce R^+ ions. As well as other high oxidant species (peroxide radicals), they are reported to be responsible for the photodegradation of organic dyes. Multiple initial reactive species, including $^1O_2$, $H^{\cdot}$, h^+, $HO^{\cdot}$, and $O_2^{\cdot-}$ can be created through photocatalytic degradation methods in UV–Vis/semiconductors. The formation of $O_2^{\cdot-}$ can prevent the recombination of photogenerated charge carriers. The $HO^{\cdot}$ might be produced within the $e^- \rightarrow O_2^{\cdot-} \rightarrow H_2O_2 \rightarrow OH^{\cdot}$ way. Besides, the $OH^{\cdot}$ radicals are created by several stages of reduction $O_2^{\cdot-}$ in the process. It was reported that the water separated in subsequent molecular layers and on the TiO_2 surface has three roles (1) preserving charges (inhibiting recombination of electron-holes), (2) performing as an electron acceptor (creation of H atoms in a reaction of photoinduced electrons with protons on the surface, $-OH_2^+$), and (3) performing as an electron donor (reaction of water with photoinduced holes to produce $OH^{\cdot}$ radicals). As claimed by prior investigations (Jiang et al., 2015), the principal active oxygen species produced through photocatalytic, and oxidation reactions are $OH^{\cdot}$ and $^1O_2$ radicals, respectively. Relying on the above thoughts, we can suggest that the possibility of creating $OH^{\cdot}$ should be much higher than the $O_2^{\cdot-}$ formation. Nevertheless, $OH^{\cdot}$ is a powerful, unselective oxidant that drives to the complete or incomplete mineralization of numerous organic compounds. According to the above statements, $^{\cdot}OH$, $^1O_2$, and $O_2^{\cdot-}$ are the active species in the mechanism of photocatalytic degradation of organic dyes. Therefore, the literatures have been indicated that the reactive $^{\cdot}OH$ performs the main role and, $^1O_2$ and $O_2^{\cdot-}$ perform an insignificant role in the photocatalytic degradation of organic dyes (Tzeng et al., 2016). The $^{\cdot}OH$ may be produced by an h^+ with H_2O. The $^1O_2$ may be created by an h^+ with $O_2^{\cdot-}$ species. The $O_2^{\cdot-}$ may be formed through an e^- with O_2 and/or $^1O_2$ with e^--species (Rahimzade et al., 2021). Therefore, $^{\cdot}OH$ can help as the most essential active species in this research.

Scavenger experiments were accomplished by employing Benzoic acid (BA) for $^{\cdot}OH$, EDTA for h^+, Benzoquinone (BQ) for $O_2^{\cdot-}$, and sodium azide for $^1O_2$ to demonstrate the function of active species in the degradation of organic dyes (Rahimzade et al., 2021). As noticed in Fig. 6f, the rate of photocatalytic decomposition decreased from 72.9% to 15.2% by adding benzoic acid to the mixture, confirming that hydroxyl radicals ($^{\cdot}OH$) are the most prominent active species in the photocatalytic reactions. Regardless, the photocatalytic efficiency declined from 72.9% to 67.2%, 71.0%, and 69.9%, respectively, by adding benzoquinone, EDTA, and sodium azide to the mixture separately, illustrating the impact of $O_2^{\cdot-}$, h^+, and $^1O_2$ on the degradation of methylene blue was not significant. An electron-hole pair can be produced by illuminating visible light to the Cs_2SnI_6 photocatalyst (Sakthivel et al., 2003). Active hydroxyl radicals can be generated from the electron (e^-) and hole (h^+) reaction in the presence of water and oxygen molecules, which can recreate a role in the decolorization of organic pollutants (Wenderich & Mul, 2016). The possible mechanism to degrade methylene blue under visible light is as [33,46]:

$$Cs_2SnI_6 + h\nu \rightarrow Cs_2SnI_6{}^* + e^- + h^+ \quad (6)$$

$$h^+ + H_2O \rightarrow {}^{\cdot}OH + H^+ \quad (7)$$

$$2H_2O + 2\ h^+ \rightarrow 2H^+ + H_2O_2 \quad (8)$$

$$^{\cdot}O_2{}^- + H^+ + 2{}^{\cdot}OH \rightarrow H_2O_2 + O_2 \quad (9)$$

$$H_2O_2 \rightarrow 2{}^{\cdot}OH \quad (10)$$

$$O_2 + e^- \rightarrow {}^{\cdot}O_2{}^- \quad (11)$$

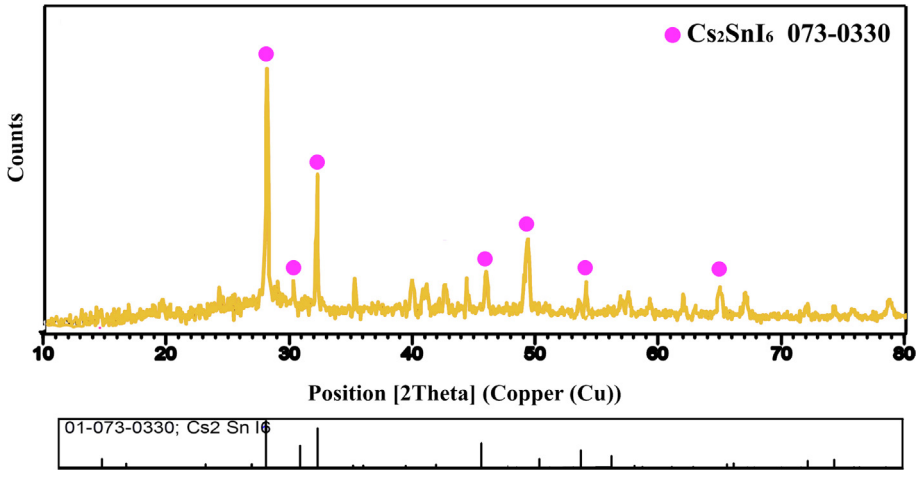

Fig. 7 XRD pattern Cs_2SnI_6 nanostructures (sample 1) after photocatalytic reaction.

Table 2 The photocatalytic performance of different iodide compounds.

Catalyst	Highest degradation (%)	Lowest degradation (%)	Catalyst dosage (mg)	Source of light	Ref.
Cs_2SnI_6 nanostructures	84.0 and 91.2% (MB)	23.7 (MO)	100	Vis	This work
Tl_4HgI_6 nanostructures	76.9 (RhB)	48.9 (ThB*)	70	UV	(Karami et al., 2021)
Cu_2HgI_4 nanostructures	92.4 (MO)	41.1 (RhB)	70	Vis	(Abkar et al., 2022)
Rb_2HgI_4 nanostructures	72.1 (AB1**)	48.1 (RhB)	70	Vis	(Abkar et al., 2021)
Tl_4CdI_6 nanostructures	85.7 (AB1)	49.1 (MB)	50	UV	(Ghanbari & Salavati-Niasari, 2018)
Tl_4PbI_6 nanostructures	72.6 (ThB)	47.8 (RhB)	50	Vis	(Rahimzade et al., 2021)
Cu_2CdI_4/CuI nanocomposites	66.0 (MB)	29.1 (MO)	50	UV	(Ghanbari et al., 2016)
Ag_2CdI_4 nanostructures	95.3 (RhB)	57.1 (AB1)	50	UV	(Ghanbari et al., 2017b)
$TlCdI_3$ nanostructures	94.6 (MB)	27.0 (MO)	50	UV	(Ghanbari et al., 2017a)

* Thymol Blue.
** Acid Black 1.

$$\cdot OH + \text{Methylene blue} \rightarrow \text{Degradation products } (CO_2, H_2O, \text{etc.}) \quad (12)$$

3.2.8. *Reusability and stability*

Cs_2SnI_6 was tested for reusability in order to determine its stability. Catalysts were centrifuged, rinsed with water, parched at 70 °C for 18 h, and then reprocessed for five periods under the same conditions. Cs_2SnI_4 exhibits remarkable durability and maintains its total photocatalytic efficiency over five cycles, as shown in Fig. 6g. Over the course of the fifth test, the photocatalytic efficiency decreased by 6.9%. Fig. 7 shows the XRD pattern of the decolorized Cs_2SnI_6 nanostructures. This figure illustrates that all diffraction peaks are coordinated with Cs_2SnI_6 (reference code: 073–0330), which has a cubic crystal structure (space group: Fm-3 m). Following the destruction of organic colorants, it may be concluded that the host composition remains intact. Cs_2SnI_6 is therefore highly stable in an aqueous solution.

3.2.9. *Comparison of photocatalytic behavior*

Table 2 compares the photocatalytic efficiency of several iodide nanostructures. In conclusion, Cs_2SnI_6 nanostructures have the potential to degrade MB efficiently, and can compete with other iodide nanostructures as photocatalysts. It is possible to introduce Cs_2SnI_6 as a new nanophotocatalyst for the treatment of water.

4. Future prospects

There has been extensive debate regarding recent developments in the fabrication of Cs_2SnI_6 nanostructures, with special emphasis on their photocatalytic properties. The presence of toxic organic dyes in wastewater generated by a variety of industries has produced undesirable contaminants in the environment. With a suitable bandgap in the visible area, Cs_2SnI_6 is a good candidate for removing toxic organic pollutants from wastewater.

5. Conclusions

A simple and rapid co-precipitation method was successfully used to fabricate Cs_2SnI_6 nanostructures. Based on the DRS results, Cs_2SnI_6 has a bandgap of approximately 1.7 eV, which is suitable for activation in the visible range. The photodecomposition of dyes revealed that Cs_2SnI_6 has a higher potential to decompose cationic dyes due to the presence of negatively charged iodide ions (I^-) in the nanostructure. As a result of photocatalytic activity, Cs_2SnI_6 decomposed 5 ppm MB approximately 84.0% in an alkaline medium after 180 min below the visible spectrum. Due to the interaction between MB as a cationic dye and SDS, removal efficiency was enhanced in the presence of SDBS (91.2%) as an anionic surfactant. According to these results, Cs_2SnI_6 alone or in combination with other semiconductors performs excellently in the visible region as a photocatalyst for the purification of water in the future.

CRediT authorship contribution statement

Fatemeh Yousefzadeh: Formal analysis, Investigation, Software, Methodology, Formal analysis. **Mojgan Ghanbari:** Investigation, Supervision, Data curation, Writing – original draft, Writing – review & editing. **Elmuez A. Dawi:** Writing – review & editing, Software, Visualization, Data curation, Validation. **Masoud Salavati-Niasari:** Formal analysis, Methodology, Writing – review & editing, Writing – original draft, Conceptualization, Supervision, Project administration, Investigation, Data curation, Validation, Resources, Visualization.

Declaration of Competing Interest

The authors declare that they have no known competing financial interests or personal relationships that could have appeared to influence the work reported in this paper.

References

Abkar, E., Ghanbari, M., Amiri, O., Salavati-Niasari, M., 2021. Facile preparation and characterization of a novel visible-light-responsive Rb2HgI4 nanostructure photocatalyst. RSC Adv. 11 (49), 30849–30859. https://doi.org/10.1039/D1RA03152J.

Abkar, E., Izadi, E., Amiri, O., Ghanbari, M., Salavati-Niasari, M., 2022. Sonochemical synthesis and characterization of Cu2HgI4 nanostructures photocatalyst with enhanced visible light photocatalytic ability. Arab. J. Chem. 15, (1) 103536.

Abrahams, S., Ihringer, J., Marsh, P., 1989. Structural and thermal dependence of normal-mode condensations in K2TeBr 6. Acta Crystallogr. B 45 (1), 26–34.

Ajibade, P.A., Oluwalana, A.E., 2021. Enhanced photocatalytic degradation of ternary dyes by copper sulfide nanoparticles. Nanomaterials 11 (8), 2000.

Al Kausor, M., Chakrabortty, D., 2021. Graphene oxide based semiconductor photocatalysts for degradation of organic dye in waste water: a review on fabrication, performance enhancement and challenges. Inorg. Chem. Commun. 129, 108630.

Amat, A., Mosconi, E., Ronca, E., Quarti, C., Umari, P., Nazeeruddin, M.K., Gratzel, M., De Angelis, F., 2014. Cation-induced band-gap tuning in organohalide perovskites: interplay of spin–orbit coupling and octahedra tilting. Nano Lett. 14 (6), 3608–3616.

Anderson, M.T., Greenwood, K.B., Taylor, G.A., Poeppelmeier, K. R., 1993. B-cation arrangements in double perovskites. Prog. Solid State Chem. 22 (3), 197–233.

Arunachalam, P., Nagai, K., Amer, M.S., Ghanem, M.A., Ramalingam, R.J., Al-Mayouf, A.M., 2021. Recent developments in the use of heterogeneous semiconductor photocatalyst based materials for a visible-light-induced water-splitting system—A brief review. Catalysts 11 (2), 160.

Attfield, J.P., Lightfoot, P., Morris, R.E., 2015. Perovskites. Dalton Trans. 44 (23), 10541–10542.

Carswell, A.D., O'Rea, E.A., Grady, B.P., 2003. Adsorbed surfactants as templates for the synthesis of morphologically controlled polyaniline and polypyrrole nanostructures on flat surfaces: from spheres to wires to flat films. J. Am. Chem. Soc. 125 (48), 14793–14800.

Chen, K., Zhang, T., Chen, X., He, Y., Liang, X., 2018. Model construction of micro-pores in shale: a case study of Silurian Longmaxi Formation shale in Dianqianbei area, SW China. Petroleum Exploration Dev. 45 (3), 412–421. https://doi.org/10.1016/S1876-3804(18)30046-6.

Chung, I., Song, J.-H., Im, J., Androulakis, J., Malliakas, C.D., Li, H., Freeman, A.J., Kenney, J.T., Kanatzidis, M.G., 2012. CsSnI3: semiconductor or metal? High electrical conductivity and strong near-infrared photoluminescence from a single material. High hole mobility and phase-transitions. J. Am. Chem. Soc. 134 (20), 8579–8587.

de Luna, M.D.G., Flores, E.D., Genuino, D.A.D., Futalan, C.M., Wan, M.-W., 2013. Adsorption of Eriochrome Black T (EBT) dye using activated carbon prepared from waste rice hulls—Optimization, isotherm and kinetic studies. J. Taiwan Inst. Chem. Eng. 44 (4), 646–653. https://doi.org/10.1016/j.jtice.2013.01.010.

Fu, F., Gao, Z., Gao, L., Li, D., 2011. Effective adsorption of anionic dye, alizarin red S, from aqueous solutions on activated clay modified by iron oxide. Ind. Eng. Chem. Res. 50 (16), 9712–9717.

Ghanbari, M., Ansari, F., Salavati-Niasari, M., 2017a. Simple synthesis-controlled fabrication of thallium cadmium iodide nanostructures via a novel route and photocatalytic investigation in degradation of toxic dyes. Inorg. Chim. Acta 455, 88–97.

Ghanbari, M., Gholamrezaei, S., Salavati-Niasari, M., Abbasi, A., 2017b. Synthesis and characterization of Ag_2CdI_4 nanoparticles and photo-degradation of organic dyes. J. Mater. Sci. Mater. Electron. 28 (8), 6272–6277.

Ghanbari, M., Salavati-Niasari, M., 2018. Tl4CdI6 nanostructures: facile sonochemical synthesis and photocatalytic activity for removal of organic dyes. Inorg. Chem. 57 (18), 11443–11455.

Ghanbari, M., Sabet, M., Salavati-Niasari, M., 2016. Synthesis of different morphologies of Cu_2CdI_4/CuI nanocomposite via simple hydrothermal method. J. Mater. Sci. Mater. Electron. 27 (10), 11092–11101.

Henkel, W., Pelzl, J., Höck, K., Thomas, H., 1980. Elastic constants and softening of acoustic modes in A2MX6-crystals observed by Brillouin scattering. Zeitschrift für Physik B Condensed Matter 37 (4), 321–332.

Islam, A., Teo, S.H., Taufiq-Yap, Y.H., Ng, C.H., Vo, D.-V.-N., Ibrahim, M.L., Hasan, M.M., Khan, M.A.R., Nur, A.S., Awual, M.R., 2021. Step towards the sustainable toxic dyes removal and recycling from aqueous solution-A comprehensive review. Resour. Conserv. Recycl. 175, 105849.

Jiang, Y.-R., Lin, H.-P., Chung, W.-H., Dai, Y.-M., Lin, W.-Y., Chen, C.-C., 2015. Controlled hydrothermal synthesis of BiOxCly/BiOmIn composites exhibiting visible-light photocatalytic degradation of crystal violet. J. Hazard. Mater. 283, 787–805.

Karami, M., Ghanbari, M., Alshamsi, H.A., Rashki, S., Salavati-Niasari, M., 2021. Facile fabrication of Tl 4 HgI 6 nanostructures as novel antibacterial and antibiofilm agents and photocatalysts in the degradation of organic pollutants. Inorg. Chem. Front. 8 (10), 2442–2460.

Khan, M.E., 2021. State-of-the-art developments in carbon-based metal nanocomposites as a catalyst: photocatalysis. Nanoscale Advances 3 (7), 1887–1900.

Kubra, K.T., Salman, M.S., Hasan, M.N., 2021. Enhanced toxic dye removal from wastewater using biodegradable polymeric natural adsorbent. J. Mol. Liq. 328, 115468.

Kumar, A., Singh, R., Kumar, S., Charaya, M., 2021. Biosorption: the removal of toxic dyes from industrial effluent using phytobiomass-A review. Plant Arch 21, 1320–1325.

Kumari, P., Meena, A., 2020. Green synthesis of gold nanoparticles from Lawsoniainermis and its catalytic activities following the Langmuir-Hinshelwood mechanism. Colloids Surf A Physicochem Eng Asp 606, 125447.

Lavanya, C., Rajesh, D., Sunil, C., Sarita, S., 2014. Degradation of toxic dyes: a review. Int. J. Curr. Microbiol. App. Sci. 3 (6), 189–199.

Lee, B., Stoumpos, C.C., Zhou, N., Hao, F., Malliakas, C., Yeh, C.-Y., Marks, T.J., Kanatzidis, M.G., Chang, R.P., 2014. Air-stable molecular semiconducting iodosalts for solar cell applications: Cs2SnI6 as a hole conductor. J. Am. Chem. Soc. 136 (43), 15379–15385.

Li, S., Wang, C., Cai, M., Liu, Y., Dong, K., Zhang, J., 2022a. Designing oxygen vacancy mediated bismuth molybdate (Bi_2MoO_6)/N-rich carbon nitride (C_3N_5) S-scheme heterojunctions for boosted photocatalytic removal of tetracycline antibiotic and Cr (VI): Intermediate toxicity and mechanism insight. J. Colloid Interface Sci.

Li, S., Wang, C., Liu, Y., Cai, M., Wang, Y., Zhang, H., Guo, Y., Zhao, W., Wang, Z., Chen, X., 2022b. Photocatalytic degradation of tetracycline antibiotic by a novel $Bi_2Sn_2O_7$/Bi_2MoO_6 S-scheme heterojunction: performance, mechanism insight and toxicity assessment. Chem. Eng. J. 429, 132519.

Liu, Z., Bai, H., Sun, D., 2011. Facile fabrication of hierarchical porous TiO2 hollow microspheres with high photocatalytic activity for water purification. Appl Catal B 104 (3–4), 234–238.

Maughan, A.E., Ganose, A.M., Bordelon, M.M., Miller, E.M., Scanlon, D.O., Neilson, J.R., 2016. Defect tolerance to intolerance in the vacancy-ordered double perovskite semiconductors Cs2SnI6 and Cs2TeI6. J. Am. Chem. Soc. 138 (27), 8453–8464.

Moller, C., 1958. Lead halide perovskite nanocreystal in the research. Nature 182, 1436.

Mora-Sero, I., Bertoluzzi, L., Gonzalez-Pedro, V., Gimenez, S., Fabregat-Santiago, F., Kemp, K.W., Sargent, E.H., Bisquert, J., 2013. Selective contacts drive charge extraction in quantum dot solids via asymmetry in carrier transfer kinetics. Nat. Commun. 4 (1), 1–9.

Nasar, A., 2021. Utilization of tea wastes for the removal of toxic dyes from polluted water—a review. Biomass Convers. Biorefin., 1–17

Pasternak, S., Paz, Y., 2013. On the similarity and dissimilarity between photocatalytic water splitting and photocatalytic degradation of pollutants. ChemPhysChem 14 (10), 2059–2070.

Peng, Y., Wang, D., Zhou, H.-Y., Xu, A.-W., 2015. Controlled synthesis of thin BiOCl nanosheets with exposed 001 facets and enhanced photocatalytic activities. CrstEngComm 17 (20), 3845–3851.

Qin, Y., Cheng, Y., Jiang, L., Jin, X., Li, M., Luo, X., Liao, G., Wei, T., Li, Q., 2015. Top-down strategy toward versatile graphene quantum dots for organic/inorganic hybrid solar cells. ACS Sustain. Chem. Eng. 3 (4), 637–644.

Qiu, X., Jiang, Y., Zhang, H., Qiu, Z., Yuan, S., Wang, P., Cao, B., 2016. Lead-free mesoscopic Cs_2SnI_6 perovskite solar cells using different nanostructured ZnO nanorods as electron transport layers. physica status solidi (RRL)–Rapid Res. Lett. 10 (8), 587–591.

Rahimzade, E., Ghanbari, M., Alshamsi, H.A., Karami, M., Baladi, M., Salavati-Niasari, M., 2021. Simple preparation of chitosan-coated thallium lead iodide nanostructures as a new visible-light photocatalyst in decolorization of organic contamination. J. Mol. Liq. 341,. https://doi.org/10.1016/j.molliq.2021.117299 117299.

Rasukkannu, M., Velauthapillai, D., Vajeeston, P., 2018. A first-principle study of the electronic, mechanical and optical properties of inorganic perovskite Cs_2SnI_6 for intermediate-band solar cells. Mater. Lett. 218, 233–236.

Sakthivel, S., Neppolian, B., Shankar, M.V., Arabindoo, B., Palanichamy, M., Murugesan, V., 2003. Solar photocatalytic degradation of azo dye: comparison of photocatalytic efficiency of ZnO and TiO_2. Sol. Energy Mater. Sol. Cells 77 (1), 65–82. https://doi.org/10.1016/S0927-0248(02)00255-6.

Santra, S., Tapec, R., Theodoropoulou, N., Dobson, J., Hebard, A., Tan, W., 2001. Synthesis and characterization of silica-coated iron oxide nanoparticles in microemulsion: the effect of nonionic surfactants. Langmuir 17 (10), 2900–2906.

Saparov, B., Sun, J.-P., Meng, W., Xiao, Z., Duan, H.-S., Gunawan, O., Shin, D., Hill, I.G., Yan, Y., Mitzi, D.B., 2016. Thin-film deposition and characterization of a Sn-deficient perovskite derivative Cs_2SnI_6. Chem. Mater. 28 (7), 2315–2322.

Sharwani, A.A., Narayanan, K.B., Khan, M.E., Han, S.S., 2021. Sustainable fabrication of silver-titania nanocomposites using goji berry (Lycium barbarum L.) fruit extract and their photocatalytic and antibacterial applications. Arab. J. Chem. 14, (12) 103456.

Shin, H., Kim, B.M., Jang, T., Kim, K.M., Roh, D.H., Nam, J.S., Kim, J.S., Kim, U.Y., Lee, B., Pang, Y., 2019. Surface state-mediated charge transfer of Cs_2SnI_6 and its application in dye-sensitized solar cells. Adv. Energy Mater. 9 (3), 1803243.

Song, X.C., Li, W.T., Huang, W.Z., Zhou, H., Yin, H.Y., Zheng, Y. F., 2015. Enhanced photocatalytic activity of cadmium-doped Bi_2WO_6 nanoparticles under simulated solar light. J. Nanopart. Res. 17 (3), 1–10.

Sui, G., Li, J., Du, L., Zhuang, Y., Zhang, Y., Zou, Y., Li, B., 2020. Preparation and characterization of g-C_3N_4/Ag–TiO_2 ternary hollowsphere nanoheterojunction catalyst with high visible light photocatalytic performance. J. Alloy. Compd. 823, 153851.

Swainson, I., Stock, C., Parker, S., Van Eijck, L., Russina, M., Taylor, J., 2015. From soft harmonic phonons to fast relaxational dynamics in $CH_3NH_3PbBr_3$. Phys. Rev. B 92, (10) 100303.

Tahir, M.B., Nawaz, T., Nabi, G., Sagir, M., Rafique, M., Ahmed, A., Muhammad, S., 2020. Photocatalytic degradation and hydrogen evolution using bismuth tungstate based nanocomposites under visible light irradiation. Int. J. Hydrogen Energy 45 (43), 22833–22847.

Tzeng, T.-W., Wang, S.-L., Chen, C.-C., Tan, C.-C., Liu, Y.-T., Chen, T.-Y., Tzou, Y.-M., Chen, C., Hung, J., 2016. Photolysis and photocatalytic decomposition of sulfamethazine antibiotics in an aqueous solution with TiO_2. RSC Adv. 6 (73), 69301–69310.

Waheed, A., Baig, N., Ullah, N., Falath, W., 2021. Removal of hazardous dyes, toxic metal ions and organic pollutants from wastewater by using porous hyper-cross-linked polymeric materials: a review of recent advances. J. Environ. Manage. 287, 112360.

Wang, X.-D., Huang, Y.-H., Liao, J.-F., Jiang, Y., Zhou, L., Zhang, X.-Y., Chen, H.-Y., Kuang, D.-B., 2019. In situ construction of a Cs_2SnI_6 perovskite nanocrystal/SnS2 nanosheet heterojunction with boosted interfacial charge transfer. J. Am. Chem. Soc. 141 (34), 13434–13441.

Wenderich, K., Mul, G., 2016. Methods, mechanism, and applications of photodeposition in photocatalysis: a review. Chem. Rev. 116 (23), 14587–14619.

Wu, T., Zhou, X., Zhang, H., Zhong, X., 2010. Bi2S3 nanostructures: A new photocatalyst. Nano Res. 3 (5), 379–386.

Xu, R., Li, J., Sui, G., Zhuang, Y., Guo, D., Luo, Z., Liang, S., Yao, H., Wang, C., Chen, S., 2022. Constructing supramolecular self-assembled porous g-C3N4 nanosheets containing thiophene-groups for excellent photocatalytic performance under visible light. Appl. Surf. Sci. 578, 152064.

Zhang, Q., Fan, W., Gao, L., 2007. Anatase TiO_2 nanoparticles immobilized on ZnO tetrapods as a highly efficient and easily recyclable photocatalyst. Appl Catal B 76 (1–2), 168–173.

Zhang, Y., Zhu, J., Li, S., Wang, J., Ren, Z., 2022. Achievement of giant cryogenic refrigerant capacity in quinary rare-earths based high-entropy amorphous alloy. J. Mater. Sci. Technol. 102, 66–71.

Zhou, P., Chen, H., Chao, Y., Zhang, Q., Zhang, W., Lv, F., Gu, L., Zhao, Q., Wang, N., Wang, J., Guo, S., 2021. Single-atom Pt-I3 sites on all-inorganic Cs_2SnI_6 perovskite for efficient photocatalytic hydrogen production. Nat. Commun. 12 (1), 4412. https://doi.org/10.1038/s41467-021-24702-8.